

Design of Capacitive Sensing Chopper Amplifier Used in Artificial Nose Detection System

Ajda Tuševski, Drago Strle

University of Ljubljana, EE dep., Ljubljana, Slovenia

Abstract: In this paper, we present the theoretical background and design procedure of a fully differentiated precision charge amplifier that can be used to detect small capacitive changes in an artificial nose detection system (ANose). We will show that with appropriate topology and optimization of circuit parameters, we can reduce $1/f$ noise and the offset and thus improve the sensitivity while keeping the power consumption at an acceptable level. Since the rate of capacitive changes due to adsorption/desorption is slow, a well-known technique such as chopping and autozeroing is used in a new way and described in the paper. The advantages and disadvantages of the proposed techniques are described. A combination of these two techniques in a single topology and new capacitive sensor ports are used to improve the detection sensitivity. Ideally, a sensitivity of $3 \text{ zF}/\sqrt{\text{Hz}}$ can be achieved, but it could be slightly worse due to various non-idealities not considered.

Keywords: Fully differential chopper amplifier 1; Capacitive sensors 2; Ripple reduction loop (RRL) 3; Artificial nose 4

Nabojni sekalni ojačevalnik za detekcijo kapacitivnih sprememb v umetnem nosu

Izveček: V članku je predstavljeno načrtovanje ter teoretičen in simulacijski postopek pri izgradnji popolnoma diferencialnega, natančnega sekalnega nabojnega ojačevalnika, ki služi zaznavanju majhnih kapacitivnih sprememb v sistemu Umetni nos. Pokazali bomo, da lahko s pravilno topologijo in optimizacijo parametrov vezja zmanjšamo $1/f$ šum in ničelno napetost ter tako izboljšamo občutljivost, hkrati pa ohranimo porabo energije na sprejemljivi ravni. Ker je hitrost kapacitivnih sprememb zaradi adsorpcije in desorpcije relativno počasna, smo uporabili tehniko sekanja in zmanjševanje ničelne napetosti in $1/f$ šuma. Ti dve tehniki sta v članku uporabljeni na nov način in bosta podrobneje opisani. V nadaljevanju sledi opis prednosti in slabosti predlagane tehnike. Kombinacija obeh tehnik sekanja v eni topologiji in nove, diferencialne kapacitivne senzorske povezave se uporabljajo za izboljšanje občutljivosti zaznavanja. Teoretični izračun kaže, da je v idealnem primeru možno doseči občutljivost $3 \text{ zF}/\sqrt{\text{Hz}}$. V realnosti pričakujemo nekoliko slabšo občutljivost, zaradi različnih neidealnosti, ki jih nismo upoštevali pri teoretičnem izračunu.

Ključne besede: Popolnoma diferencialen sekalni ojačevalnik 1; Diferencialni kapacitivni senzorji 2; RRL 3; Umetni nos 4.

*Corresponding Author's e-mail: ajda.tusevski@fe.uni-lj.si

1 Introduction

The development and optimization of a detection system for artificial nose (ANose) with increased sensitivity for measuring small changes in differential capacitance represents a significant improvement in sensor technology. The collaboration between LMFE, JSI and FKKT in improving the ANose system emphasizes the importance of interdisciplinary collaboration in improving sensor capabilities [1] - [7].

The transition from an existing ANose system with thirty differential capacitive sensor pairs and thirty ASICs [2, 7] to a new integrated system with 256 capacitive sensor pairs integrated on a single ASIC shows promising progress in sensor array technology and ANose. The integration of the electronics for all channels on a single ASIC requires the development of an extremely low-noise input charge amplifier with minimal area and low power consumption. This innovation is essential for

How to cite:

A. Tuševski et al., "Design of Capacitive Sensing Chopper Amplifier Used in Artificial Nose Detection System", Inf. Midem-J. Microelectron. Electron. Compon. Mater., Vol. 54, No. 4(2024), pp. 247–257

accurate measurements of small capacitive changes on modified capacitors due to adsorption processes.

The focus of the work is to analyze the influence of different noise sources that affect the overall noise during the measurements and to design a circuit that can improve the noise characteristics. This analysis is crucial for optimizing the noise performance of the new system. Through a detailed analysis of the chopping technique, the capacitive sensor setup and the ripple reduction loop (RRL), the paper provides valuable insights into the design considerations and techniques used to achieve high sensitivity and low noise in the ANose system. The inclusion of simulation results in the paper adds a practical dimension to the theoretical framework and demonstrates the effectiveness of the proposed design and techniques.

The article is organized as follows. Section 2 presents the basic concept of the chopping technique. A one channel of ANose with the proposed capacitive sensor and the connection of a specially arranged chopper amplifier to the differential capacitive sensor pair is discussed in Section 3. The working principle of the ripple reduction loop (RRL) is described in Section 4. Section 5 presents some simulation results, while the last section concludes the article.

2 Chopping technique

The use of the chopping technique in the amplifier design for the ANose detection system is well justified. Chopping is a well-known method for attenuating offset voltage, 1/f noise and other unwanted artifacts in CMOS amplifiers, especially when amplifying small, low-frequency signals. In the context of the ANose detection system, which involves measuring extremely small changes in the capacitance, it must be ensured that the noise contribution and offset voltage of the amplifier do not distort the small signals. By designing a chopper amplifier, the system should effectively suppress these noise sources and maintain the integrity of the measured signals, allowing accurate detection of capacitance changes caused by adsorption processes. The use of a chopper amplifier in this application is a thoughtful approach to overcoming the challenges associated with amplifying and capturing small signals in a high-precision sensor system. By taking advantage of chopping, the design can improve signal quality, increase sensitivity and minimize the effects of noise and offset voltage, optimizing the performance of the ANose sensing system to detect small capacitance changes.

For this reason, we have developed a chopper amplifier. The operating principle is shown in a simplified block diagram in Figure 1. a) [9]. The challenges associated with DC input offset voltage and 1/f noise in CMOS amplifiers are significant, especially in high-precision applications such as the ANose sensor system. To combat the effects of 1/f noise, it is critical to select a chopper frequency in the amplifier design that exceeds the 1/f noise corner frequency of the amplifier. In addition, with this approach we may also measure the noise spectrum caused by the adsorption/desorption process in a band up to several 100kHz.

In the chopper amplifier configuration, the input signal is first subjected to upward modulation, where the signal is modulated to a higher frequency. Both the 1/f noise and the offset voltage of the amplifier are then added to the high frequency modulated signal. The amplified signal, including the noise and offset, is then modulated again with the same frequency, resulting in demodulation of the signal back to a lower frequency, while the offset voltage and 1/f noise are modulated upwards. This demodulation technique effectively separates the desired signal from the unwanted noise and offset components by up-modulating the noise and offset so that they can be removed later in the process.

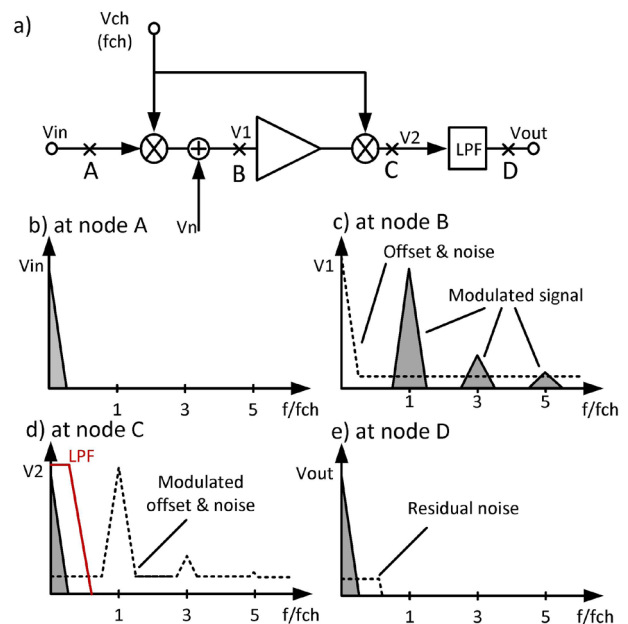


Figure 1: Simplified block diagram of chopper amplifier with spectrums in various nodes. a) Block diagram of chopper amplifier. b) Spectrum of the input signal V_{in} (node A), c) Spectrum of offset and noise together with the modulated input signal after amplification (node B), d) Spectrum after the second chopper (node C). The red shape represents the transfer function of a first order LPF filter, and e) the spectrum after the LPF (node D).

By integrating this modulation-demodulation approach into the design of the chopper amplifier, the system can effectively counteract the effects of $1/f$ noise and offset voltage of the circuit. Consequently, this strategy improves the overall quality and precision of the signals and facilitates the detection of small capacitance changes. In addition, the application of low-pass filtering in the system attenuates high-frequency components, as shown in Figure 1e). It is obvious that the chopper technique contributes to the reduction of $1/f$ noise and offset voltage when the chopper frequency exceeds the $1/f$ noise corner frequency of the amplifier. Furthermore, it is important to recognize that in practical scenarios, the level of thermal noise at the output of a chopper amplifier may slightly exceed that of a standard amplifier due to the folding of the thermal noise. In addition, charge injection effects may occur during operation of the amplifier, which must be taken into consideration [10]. To summarize, the integration of chopper amplifiers with modulation-demodulation techniques together with low-pass filtering is a powerful strategy to attenuate the noise and the offset voltage problems, ultimately improving signal quality and accuracy.

3 One channel of ANose system

Figure 2 shows the simplified circuit diagram of one channel of the measuring system amplifier, which contains several important components for accurate signal processing. The programmable input DC signal source generates two DC voltages, V_{sp} and V_{sn} , which serve as input signals to the system. These DC voltages are chopped by the input differential chopper Ch01, resulting in the square wave signals V_{in1} and V_{in2} ; chopping frequency is programmable. They are connected to a pair of capacitive differential sensors as shown in Fig-

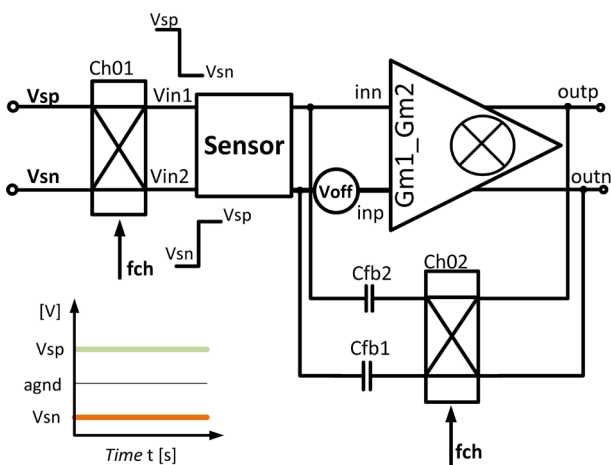


Figure 2: Charge amplifier for one channel of ANose detection system.

ure 2. The charges coming from the sensors are further processed by a low-noise charge amplifier consisting of a Gm1_Gm2 cell, which converts the charges into voltages via a feedback loop consisting of a differential chopper (Ch02) and feedback capacitors Cfb.

The arrangement of the components in this amplifier channel shows a systematic approach to signal processing and amplification. By using chopping techniques and incorporating feedback mechanisms, the amplifier design aims to increase sensitivity, reduce noise and optimize signal integrity for accurate detection of small capacitance changes in the ANose detection system. It is important to note here that the signal coming from the sensor due to capacitive changes can be several orders of magnitude smaller than offset or $1/f$ noise; fortunately, with correct signal processing it appears in different frequency band.

The integration of programmable input signals, differential chopping and a low-noise charge amplifier illustrates a comprehensive approach to signal processing in the measuring system. This design enables the precise measurements of extremely small capacitance variations and improves the overall performance and sensitivity of the ANose sensor system. The signal processing scheme shown in Figure 2 assumes that the chopping frequency exceeds the $1/f$ corner frequency of the amplifier. The signals V_{in1} and V_{in2} are square wave signals with a frequency f_{ch} and amplitudes of $V_{sp}-V_{sn}$, which represent the DC voltage difference between V_{sp} and V_{sn} . It is important to note that signals V_{in1} and V_{in2} are 180° out of phase; when V_{in1} is connected to V_{sp} , V_{in2} is connected to V_{sn} and vice versa (see Figure 3:a).

The details of the connection of the input voltages V_{in1} and V_{in2} to the capacitive differential sensor are shown in Figure 3.a. A sensor consists of two differential sensor pairs with a comb-like structure (see Fig. 3 b). Comb capacitors are covered with a thin layer of silicon dioxide. Each pair is then functionalized with different receptor molecules [1].

The measurement of sensor capacitance changes due to the adsorption of target molecules are significantly influenced by the electric field. In humid air, the breakdown voltage—where the air becomes conductive due to ionization—ranges from 5 to 10 megavolts per meter (MV/m). For 1 μm space between fingers of comb sensors capacitors and sensing voltage of 5V, we are already at the limit. However, it is possible to reduce the sensing voltage but then also the sensitivity is reduced. In addition, the gap between fingers cannot be smaller because of sensor functionalization technology. This is the main reason why 180 nm CMOS technology is good for our detection system.

Assuming that surface of C_p is functionalized, and surface of C_n is not functionalized, the adsorption of target molecules changes the capacitance C_p , while the capacitance C_n remains the same. The capacitance changes due to adsorption are represented by C_{ads1} and C_{ads2} on Figure 3.a. The signal connection structure ensures that the differential signal generated by the sensor pair is effectively detected and processed by the differential charge amplifier, so that the charges at the output of the charge amplifier are effectively converted into differential voltage. To detect these small differential capacitance changes, each part of the sensor is divided into two parts to extract differential charges across the inn and inp nodes.

By organizing the sensor structure in this way, two pairs are formed as shown in Figure 3. The first pair includes

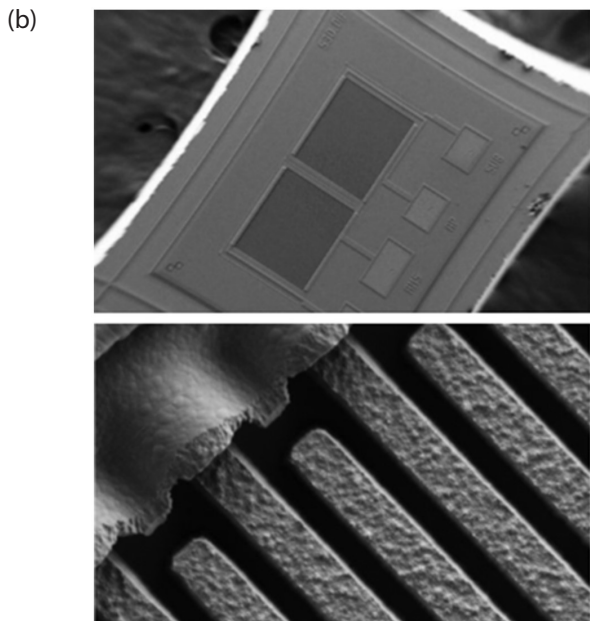
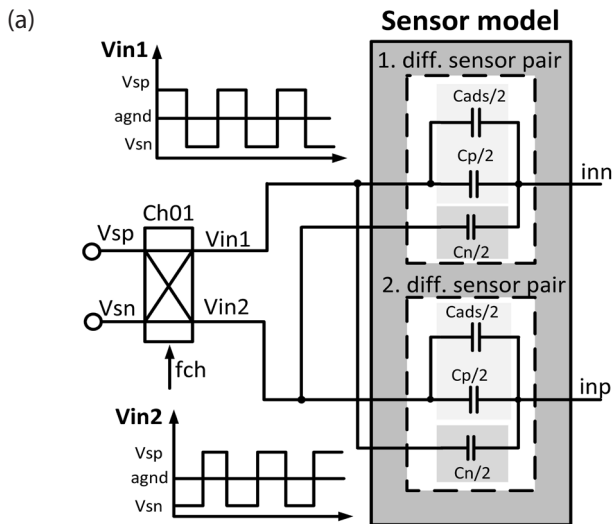


Figure 3: a) Differential capacitive pair connection; b) Comb capacitive sensor.

$C_{p1} + C_{ads1}$ and C_{n1} , while the second pair consists of $C_{p2} + C_{ads2}$ and C_{n2} . In addition, the signals V_{in1} and V_{in2} are connected to the differential sensor pairs, as shown in Figure 3. V_{in1} is connected to a node consisting of capacitors C_{ads1} and C_{p1} , while V_{in2} is connected to a node with C_{n1} . In the second differential sensor pair, the V_{in2} signal is connected to C_{ads2} and C_{p2} , while V_{in1} is connected to C_{n2} .

At this point we assume that $V_{sp} - V_{agn} = V_{agn} - V_{sn} = V_s$, so that the charges in time $(n-1)$ and (n) at the first differential sensor pair at inn and assuming that the sensors are connected to the virtual ground of the charge amplifier are (1) and (2):

$$q(n-1) = (V_s(n-1) - V_{agn}) \cdot (C_{ads1} + C_{p1} - C_{n1}) \quad (1)$$

$$q(n) = (V_s(n) - V_{agn}) \cdot (C_{n1} - C_{ads1} - C_{p1}) \quad (2)$$

Charges in time $(n-1)$ and (n) on the second differential sensor pair on inp are given by (3) and (4):

$$q(n-1) = (V_s(n-1) - V_{agn}) \cdot (C_{n2} - C_{ads2} - C_{p2}) \quad (3)$$

$$q(n) = (V_s(n) - V_{agn}) \cdot (C_{ads2} + C_{p2} - C_{n2}) \quad (4)$$

Now let's take a closer look at the signals in the time domain and parts of the charge amplifier. For one differential capacitive pair, and if $V_{sp} = -V_{sn} = V_s$, we can calculate the voltage step V_{in1} on one capacitor pair according to (5):

$$V_{in1} = V_{sp} - V_{sn} = 2 V_s = \Delta V_{in} \quad (5)$$

The same is true for the second differential pair (6):

$$V_{in2} = -V_{sn} - V_{sp} = -2 V_s = -\Delta V_{in} \quad (6)$$

$$|V_{in1}| = |V_{in2}| = \Delta V_{in} \quad (7)$$

The signals V_{in1} and V_{in2} , generated after the first chopper in the circuit in Figure 3, have rectangular shapes with a step size of ΔV_{in} , as suggested in (5), (6) and (7). These waveforms consist of transitions between two different voltage levels, resulting in a square wave or a rectangular waveform at the output. The step size ΔV_{in} indicates that the amplitude is the difference between the high and low voltage levels V_{sp} and V_{sn} . Assuming an ideal amplifier (block $G_{m1_G_{m2}}$) with an offset voltage of zero and assuming that $C_p = C_n$ and $C_{ads} = 0$ and also that the nodes inn and inp are at virtual ground potential, the charge conservation equation for the simplified single-ended circuit during the transition of the input signal from low to high at V_{inp}

(or from high to low at V_{inn}) can be expressed as equation (8):

$$\begin{aligned} & \left[\Delta V_{in} \cdot (C_{p1} + C_{ads1}) - \Delta V_{in} \cdot C_{n1} \right] + \\ & + \left[(V_{outn}(n) - V_{outn}(n-1)) \cdot C_{fb1} \right] = 0 \end{aligned} \quad (8)$$

For $C_{ads}=0$ the output voltages are equal, therefore:

$$V_{outn}(n) = V_{outn}(n-1)$$

At the transition from high to low, the circuit behaves similarly to the transition from low to high, but with reversed polarity, since the input voltage jump by $-\Delta V_{in}$, and thus the changes in the output voltages also have reversed signs. If the capacitances C_{ads1} and/or C_{ads2} are no longer zero, the output voltages are also no longer zero:

$$V_{outp}(n) = V_{outp}(n-1) + \frac{C_{ads1}}{C_{fb2}} \Delta V_{in} \quad (9)$$

$$V_{outn}(n) = V_{outn}(n-1) - \frac{C_{ads2}}{C_{fb1}} \Delta V_{in} \quad (10)$$

Looking differentially and if $C_{fb2} = C_{fb1} = C_{fb}$:

$$V_{out_{diff}}(n) = V_{out_{diff}}(n-1) + \Delta V_{in} \cdot \frac{C_{ads1} + C_{ads2}}{C_{fb}} \quad (11)$$

The differential output voltage is proportional to ΔV_{in} and the ratio between $(C_{ads1} + C_{ads2})$ and C_{fb} .

The first sub cell within the amplifier block $gm1_gm2$, called $gm1$, acts as a transconductance amplifier. This sub-cell converts the input voltage applied to node inn into an output current as defined in equation (12).

$$i_p \cong \left(\frac{C_{ads1} \Delta V_{in}}{C_{fb2} A} \right) \cdot g_{m1} \quad (12)$$

Table 1: Value of charge amplifier parameters.

Parameters of charge amplifier			
Cads	100fF	Cp1, Cp2	200fF
Ain	1V	Cn1, Cn2	200fF
vdd	5V	R1, R2	30kΩ
Voff	5m	Cint1, Cint2	250fF
agnd	2.5V	Cfb ₁ , Cfb ₂	200fF
Vsp	3.5V	fch	1M
Vsn	1.5V		

It is assumed that the influence of the parasitic capacitance at the inn node on the circuit is negligible, assuming ideal behavior in the time domain. The expression containing $gm1$ as the trans-conductance of the first stage and A as the ideal open-loop gain of the entire amplifier $gm1_gm2$ refers to the operating characteristics of the amplifier block. A similar expression applies to the input inp . The chopper $Ch02$ reverses the connection of ip and in into two integrator stages; they convert currents to voltages and at the same time serve as low-pass filters. The voltage at the output of the integrator is calculated from equation (13):

$$\begin{aligned} V_{outp}(t) &= V_{outp}(0) + \frac{i_p \cdot t}{C_{int2}} = \\ &= V_{outp}(0) + \frac{\left(\frac{C_{ads1} \Delta V_{in}}{C_{fb2}} / A \right) \cdot g_{m1} \cdot t}{C_{int2}} \end{aligned} \quad (13)$$

Since $i_p = -i_n$, the voltages V_{outp} and V_{outn} at the end of $T_{chp}/2$ are $V_{outp} = -V_{outn}$. This condition indicates an antiphase relationship between the output voltages at the end of the first half of the chopping period. At the transition from (inn, inp) to $(outp, outn)$, the cell $gm1_gm2$ acts as a voltage amplifier, with V_{outp} and V_{outn} representing integrated versions of the output currents (i_p, i_n) derived from $gm1$.

The common mode feedback loop (CMFB) serves as a correction mechanism for the common mode output voltage. By using two integrators in the circuit design, the currents i_p and i_n are effectively converted into two voltages. Up to this point, we have neglected the offset voltage of the amplifier. If we add the model of the offset voltage of $gm1$ to equations (12) and (13), we obtain equation (14). This equation gives a more detailed insight into the total output current (i_p, i_n), taking into account the characteristics of the transconductance and the effects of the offset voltage of the $gm1$ amplifier.

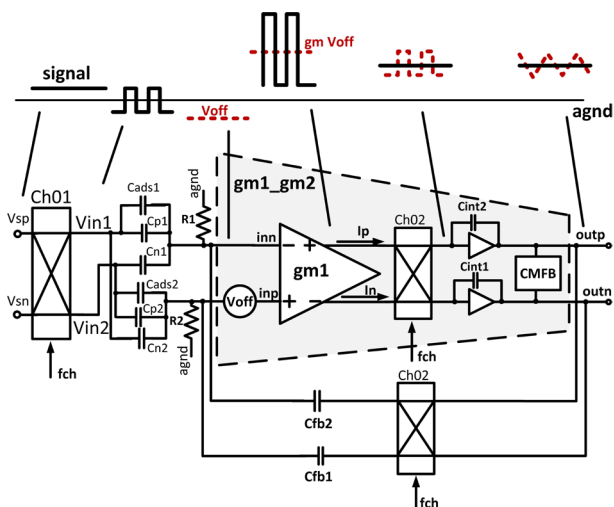


Figure 4: Charge amplifier with signals in the time domain. Black signals are caused by C_{ads} , while signals in red are due to the offset voltage of the op-amp.

$$i_p = \left(\frac{\frac{C_{ads1} \Delta V_{in}(t)}{C_{fb2}}}{A} \right) \cdot g_{m1} + \frac{V_{off}}{2} \cdot g_{m1} \quad (14)$$

The current i_p is now made up of both the direct current component (DC), which is caused by the offset, and the alternating current component (AC), which is caused by the input voltage. This combined current is then chopped with ChO2, a component that reverses the connection of the currents to two output stages. Under ideal conditions, the process is equivalent to multiplying each signal by ± 1 , so that the measured signal is down sampled, and the offset is up-sampled. See Figure 4 for time domain signals and Table 1 for values of simulation parameters. The voltages V_{outp} and V_{outn} at time t are calculated according to equation (15):

$$V_{outp}(t) = V_{outp}(0) + \frac{C_{ads1} g_{m1} \Delta V_{in} t}{C_{fb2} C_{int2} A} + \frac{v_{off} g_{m1} t}{C_{int2}} \quad (15)$$

Equation (18) represents the complete output voltage, (16) represent the DC part, while (17) represent the V_{AC} part.

$$V_{DC} = \frac{C_{ads1} g_{m1} \Delta V_{in}}{C_{fb2} C_{int2} A} t \quad (16)$$

$$V_{AC} = \frac{v_{off} g_{m1}}{C_{int2}} t \quad (17)$$

$$V_{outp}(t) = V_{outp}(0) + V_{DC} + V_{AC} \quad (18)$$

V_{DC} is contribution of C_{ads1} and V_{AC} is contribution of the offset voltage (v_{off}) and the $1/f$ noise of the gm1 cell.

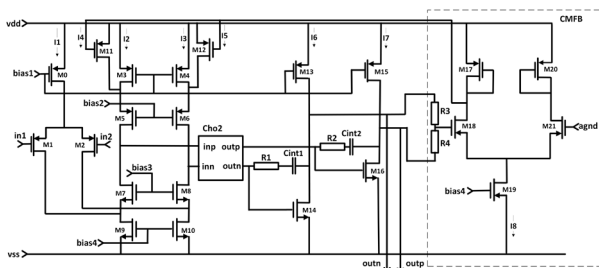


Figure 5: Simplified circuit diagram of gm1_gm2 cell.

Figure 5 shows simplified circuit diagram of gm1_gm2 cell. It is built as modified folded cascode amplifier that implements a gm1 part of the cell using PMOS folded cascode circuit. The output currents are chopped using chopper Cho2, which is constructed from CMOS switches, followed by two integrator stages. The common mode feedback amplifier (CMFB) controls the common-mode output voltage levels through the gm1

stage. The value of transistors dimensions, supply current, bias voltage and passive component of gm1_gm2 cell are presented in Table 2.

The ripple caused by the offset voltage, which is transferred to frequency f_{ch} , can significantly affect the signal quality and accuracy.

Table 2: Dimensions of transistors, supply current, bias voltages and passive components of gm1_gm2 cell.

Parameters of gm1_gm2 cell			
Mo	16 $\frac{10u}{2u}$	R1, R2	5kΩ
M1, M2	4 $\frac{24u}{1u}$	R3, R4	1.5MΩ
M3, M4	12 $\frac{10u}{2u}$	bias1	4V
M5, M6	16 $\frac{10u}{0.5u}$	bias2	3.668V
M7, M8	16 $\frac{8u}{1u}$	bias3	1.187V
M9, M10	24 $\frac{8u}{2u}$	bias4	0.9V
M11, M12	4 $\frac{10u}{2u}$	I1	80uA
M13, M15	32 $\frac{10u}{2u}$	I2, I3	60uA
M14, M16	8 $\frac{8u}{1u}$	I4, I5	20uA
M17, M20	4 $\frac{10u}{2u}$	I6, I7	160u
M18, M21	4 $\frac{4u}{1u}$	I8	40u
M19	8 $\frac{8u}{2u}$	agnd	2.5V
vdd	5V	vss	0V

For example, if we have an offset voltage of 10mV, the amplitude of the AC voltage at the chopping frequency for $f_c=1$ MHz, transconductance of 0.1mS and $C_{int}=10$ pF, the calculated output AC voltage, also known as ripple voltage, is 50mV. To attenuate or remove this ripple caused by the offset voltage (and $1/f$ noise), we could use LP filtering, however more efficient and better technique is so called ripple reduction loop (RRL), that will be described in the next section.

3.1 Ripple reduction loop

The ripple at the output due to the modulated offset and $1/f$ noise of the transconductance amplifier cell gm1 is undesirable as it can affect the accuracy and

performance of the system, especially in applications with low frequency signals such as ANose. There are several effective techniques to mitigate this ripple, such as filtering techniques and other suppression techniques described in the literature [9], [10]. It is crucial to address this issue as excessive ripple can eat up headroom and degrade the quality of the output signals. One approach to reduce the ripple is the ripple reduction loop (RRL) shown in Figure 6 and the value of parameters are listed in Table 3.

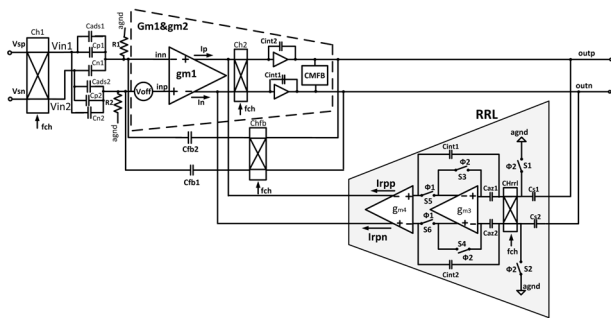


Figure 6: RRL that consists of sensing capacitors Cs1, Cs2, a demodulating chopper CHr1, autozeroed S-C integrator and a compensation transconductor gm4.

Table 3: Parameters of RRL that are used in simulation.

Parameters of RRL			
Caz1, Caz2	33fF	Cint1 _{RRL} , Cint2 _{RRL}	33fF
Cs1, Cs2	33fF	fch	1MHz

RRL is specifically designed to detect the ripple at the output of the voltage amplifier. As soon as the ripple is detected, the RRL generates compensating currents to compensate the DC offset current generated by the transconductance amplifier gm1. Ideally, it is possible to reduce the ripple completely. In the ideal case, the output ripple of the signals Voutp and Voutn should no longer be present after using the RRL technique [8].

Ripple voltage at the output without RRL can be calculated from equation (19):

$$V_{\text{ripple}} = \frac{(V_{\text{offset}} \cdot g_{m1})}{(2 \cdot f_{\text{chop}} \cdot C_{\text{int}})} \quad (19)$$

The ripple caused by the offset voltage can be reduced by decreasing gm1 or increasing Cint. Since reducing gm1 can lead to increased noise, this approach is not effective. Adjusting parameters such as chopping frequency (fch) and integration capacitance (Cint) can affect the residual offset, chip area and power consumption. By using the RRL technique, the system can effectively suppress the output ripple and improve the overall performance and stability of the charge amplifier.

In this paper, an AC-coupled discrete-time ripple reduction loop (RLL) is presented. The block diagram and the components of the ripple reduction loop (RRL) are shown in Figure 6. This diagram illustrates how the RLL is structured, and which are the main components involved in the ripple reduction process.

The ripple reduction loop (RRL) consists of the following important components:

- i. Sensing capacitors (Cs1,2). These capacitors Cs1,2 sense and convert the large ripple voltage at the amplifier’s output into an AC current, which is proportional to the slope of the ripple.
- ii. A demodulating chopper (CHr1). The demodulating chopper processes the AC current generated by the sensing capacitors, helping to extract and isolate the ripple component for further signal processing
- iii. An integrator. It is utilized to integrate the AC current signal, acting as a low-pass filter to smooth out the ripple and convert it into a voltage signal proportional to the ripple amplitude. It serves also as S/H stage.
- iv. A compensation trans-conductor gm4. It receives the voltage signal from the integrator and generates compensating currents to compensate the effects of the ripple in the output signals.

The RRL generates a notch at frequency fch with a width determined by flexible design parameters such as Cs1,2 and gm4 [8]. A passive integrator consisting of a current buffer and an integration capacitor used in the RRL has the offset of the current buffer, which produces a second harmonic ripple that would require a large integration capacitor for filtering [10], [11]. In our system, we designed an integrator with automatic zeroing and switched capacitor (see Figure 6), as this is a common technique used in precision analog circuits to reduce offset errors. In this design approach, the integrator is reset during one phase of the operating cycle so that its offset voltage is stored on a self-zeroing capacitor (Caz1,2). The implementation of a self-zeroing switched capacitor (SC) integrator in the circuit enables periodic storage and clearing of the offset voltage. This process minimizes the offset error of the integrator and the S/H stage and improves the accuracy of the circuit by effectively reducing the unwanted voltage offsets of the RRL. However, it is essential to note that the output of the integrator must not be connected to gm4 during the integration phase of the offset cancellation. If such a connection is made, there is a risk that error-compensating currents will be fed into the voltage amplifier (block gm1&gm2). During this time, the voltage at the input of gm4 is kept constant by the voltage stored in the capacitors Cint1 and Cint2.

The SC integrator consists of sampling capacitors $C_{s1,2}$, a demodulation chopper CH_{rrl} , integration capacitors $C_{int1,2}$, auto-zero capacitors $C_{az1,2}$ and a single-stage operational amplifier gm_3 . CH_{rrl} is synchronised with f_{ch} , and the remaining switches (S_1 - S_6) are controlled with the switching frequency f_{az} , which is set to half of f_{ch} (see Figure 7). The signal f_{az} contains an integration phase Φ_1 and an auto-zero phase Φ_2 , and each phase comprises a complete cycle of f_{ch} . Thus, a ripple can be detected and stored by the full-cycle ripple reduction loop (RRL) operation during Φ_1 . A timing diagram is shown in Figure 7.

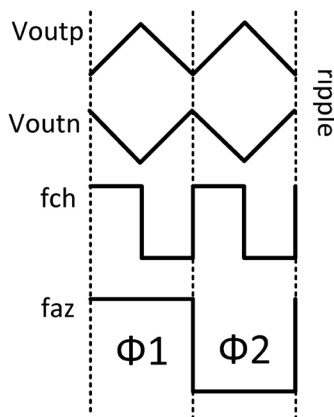


Figure 7: Timing diagram of output ripple, chopping frequency (f_{ch}) and auto zeroing frequency (f_{az}), which is set to half of f_{ch} .

During Φ_1 , $C_{s1,2}$ plays a critical role in the operation of the circuit by converting the ripple voltage into an alternating current. This alternating current is further processed by demodulation of CH_{rrl} (a demodulating chopper). The demodulated signal is then integrated at C_{int1} and C_{int2} . The voltages at capacitors C_{int1} and C_{int2} are used to drive gm_4 , which converts the differential voltage into two currents to compensate for the offset current of gm_1 . During phase 2 (Φ_2), the measuring capacitors $C_{s1,2}$ are short-circuited to the analog ground so that no ripple current can be integrated. At the same time, the input voltage at gm_4 is kept at a constant level, as the voltages at C_{int1} and C_{int2} are kept constant during this phase.

This configuration ensures that no additional ripple current is introduced or integrated during Φ_2 and the input voltage at gm_4 remains stable. gm_3 is configured in the unity gain configuration so that its offset is sampled and stored on $C_{az1,2}$. During this time, C_{int1} and C_{int2} are disconnected from the output of gm_3 , hold the voltage set at the end of the last Φ_1 and are connected to the input of gm_4 . In this way, the correct compensation current is fed into gm_1 in both phases. Ideally, the compensation current fully compensates the offset current of gm_1 so that no output ripple occurs in the steady state.

Before looking at the simulation results, let's calculate SnR and minimum capacitance that can be detected using proposed charge amplifier. Assume the BW is 1Hz, $C_{ads} = 100\text{fF}$, $C_p = C_n = 200\text{fF}$, $V_{ndth_in} = 10\text{nV}$. RMS signal and RMS noise at the output of the charge amplifier can be calculated from equations (20) and (21):

$$V_{\text{sout_RMS}} = \frac{V_{\text{in}} \cdot C_{\text{ads}}}{\sqrt{2} \cdot C_{\text{fb}}} \tag{20}$$

$$V_{\text{ndout_RMS}} = V_{\text{ndth_in}} \left(1 + \frac{C_{\text{ads}} + C_p + C_n}{C_{\text{fb}}} \right) \tag{21}$$

The calculated SnR for the proposed conditions is 140dB/√Hz. The minimum capacitance that can be detected, is thus $C_{\text{ads}} \geq 2.82 \cdot zF/\sqrt{\text{Hz}}$.

4 Simulation results

The presented topology of a fully differential capacitive coupled chopper amplifier with a differential capacitive sensor pair at the input and RRL was simulated in Cadence using TSMC's 180nm CMOS technology PDK.

The simulation consists of the same blocks as shown in Figure 6. First, a capacitively coupled charge amplifier is simulated when the RRL is switched off. The ripple at the output of the charge amplifier is mainly caused by the offset voltage of the transconductance amplifier gm_1 . In the simulation, we set the offset voltage of gm_1 to 5mV, which corresponds to the typical offset of CMOS amplifiers, $C_{\text{ads}} = 0\text{fF}$, $V_{\text{in}} = 1\text{V}$, $f_{\text{ch}} = 1\text{MHz}$, $gm_1 = 0.1\text{mS}$ and $C_{\text{int}} = 10\text{pF}$. The calculated output voltage ripple from equation (19) is $V_{\text{ripple}} = 25\text{mV}$ and the measured voltage ripple from the simulation is 26mV, which is almost identical (see Figure 8 and Table 4).

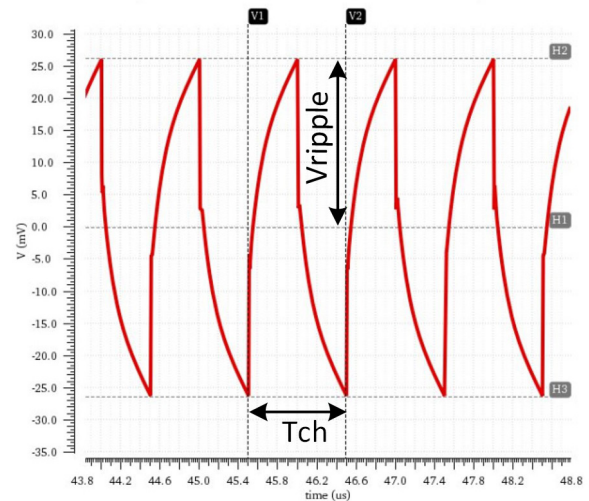


Figure 8: Differential signal at output of charge amplifier without RRL and with C_{ads} is 0.

Figure 9 shows the result (output voltages) when RRL is switched on. It can be seen that RRL can suppress the ripple caused by the offset voltage of gm1 by a factor of approx. 100. If you enlarge the diagram in Figure 9a, you can see that some ripple is still present (see Figure 9b).

The measured ripple is 0.00038 V, as shown in Table 4 in the third row. Then we performed another simulation when Cads was no longer zero. The DC output voltages (see Figure 9 and Figure 10) are calculated using equations (9) and (10). The data used for the simulations are $V_{in} = 1V$, $C_{ads1} = C_{ads2} = 100fF$ and $C_{fb1} = C_{fb2} = 200fF$ and the signal ground is $V_{dd}/2 = 2.5V$. The DC output voltages are 3V and 2V, i.e. 0.5V, which are different. First, we simulated the system when RRL was switched off.

And then we did a simulation when RRL was switched on. The measured voltage ripple without RRL is 26mV

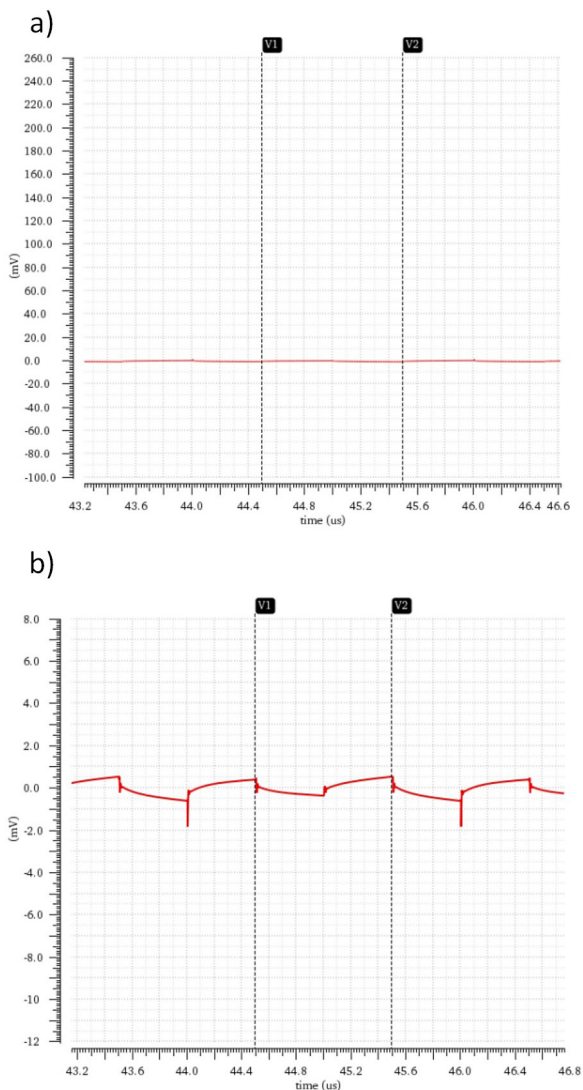


Figure 9: a) Simulation result at the output of the charge amplifier with RRL and with Cads is 0. b) The second graph is a zoom of the first graph in y direction.

and the measured voltage ripple with RRL is 0,3mV.

The ripple reduction loop (RRL) reduces the ripple voltage by at least a factor of 100, which is the main reason why the RRL is indispensable in our system on a chip. Table 4 shows the different voltage ripples and differential output voltages when changing the values of Cads without RRL and with RRL. It can be seen from Table 4 that RRL effectively suppresses the ripple voltage caused by the offset voltage of a gm1 cell.

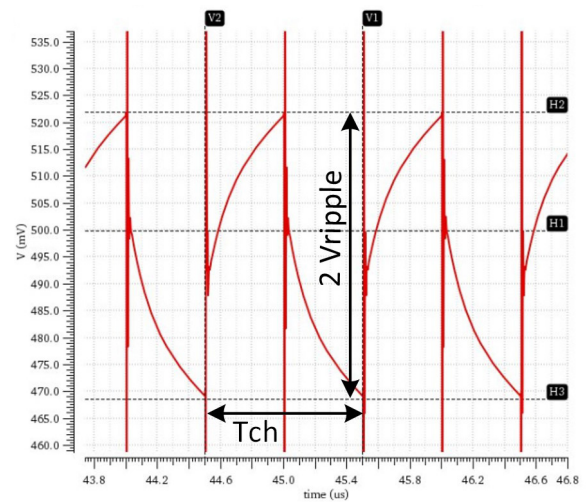


Figure 10: Differential signal at outputs of the charge amplifier without RRL and Cads is set to 100fF.

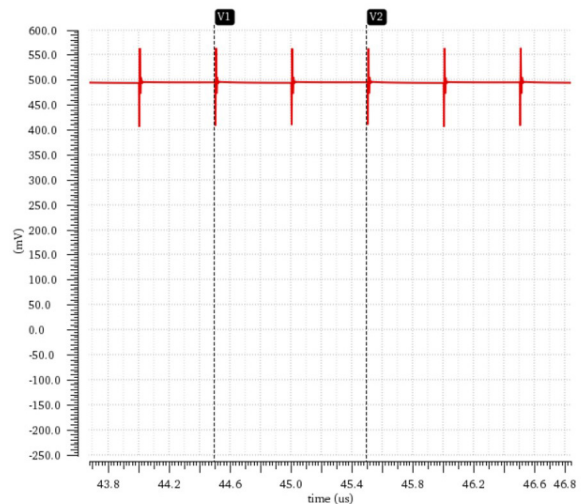


Figure 11: Simulation result at outputs of the charge amplifier with RRL and Cads is set to 100fF.

Table 4: Different values of Cads without and with RRL.

	Cads	RRL	Vripple	Vdiff
1.	Off	No	0.02608V	0V
2.	100fF	No	0.02634V	0,52V
3.	0fF	Yes	0.00038V	0V
4.	100fF	Yes	0.0003V	0,49V

If we compare the above results with the results from article [8], we find that our system without including RRL has a 10x lower output ripple voltage (V_{ripple}). That means that if we suppress the output ripple voltage by 100x with added RRL, we are left with output ripple voltage in the order of microvolts.

In last decade, a lot of work has been done in field of offset compensation. Article [8] presents a low-power precision instrumentation amplifier for use in wireless sensor nodes with ripple reduction loop, positive feedback loop and DC servo loop. Chip was fabricated in 65nm technology with fixed gain of 100 and BW in Hz, with low supply voltage (1V) and current (1.8uA). They achieve reduction of output ripple by 1000x. The article [12] proposes the use of a so-called fill-in technique to eliminate IMD pulses in chopper amplifiers that is caused by the interaction between the input signal and the chopper clock. The chip was made in 180nm BCD process with 5V supply voltage and 0.55mA with GBW of 4.2MHz with fin of 79kHz. Reported results for fin = 79kHz with fill-in technique is -125.9dB at 1kHz. Article [13] describes amplifier for electroretinography (ERG) and new method dynamic offset zeroing for reduction of large unwanted ripple. The chip was fabricated in 0.18um technology, with supply voltage of (0.5 -1.8) V with 7uA supply current. The gain of the system is 60dB and BW of 300Hz. The reported residual ripple in rms is 6mV.

The comparison of results from the literature with our own circuit is difficult, since we try to measure extremely small capacitive changes, while in other work different quantities are measured. However, comparing the remaining ripple of our circuit with the work of [8] shows that, the remaining ripples are similar. Furthermore, the circuitry described in [8] and [13] have smaller bandwidth, compared to ours. The article [12] talks about suppression of CH-induced unwanted IMD tone at a certain frequency, depending on input signal frequency and can not be directly compared with our system.

Our system measures extremely small differential capacitive changes with sensitivity in a range of zF/\sqrt{Hz} with programmable bandwidth in a range of several 100kHz. We think that our simulation results shows that we constructed good system with suppressed ripple by factor of 100x, which means that we are left with less than 0.3mV ripple at the output. This motivates us for future research and system improvements.

5 Conclusions

In this paper, we present the first steps towards building a precision artificial nose detection system comprising 256 differential capacitive pairs and complete

front-end electronics for all channels on a single ASIC. The presented topology of capacitive sensors and chopper amplifier with a proposed new topology for differential capacitive sensors is the main contribution. However, the topology requires further optimization.

Other performance parameters need to be addressed and carefully simulated. One of them is the noise characteristics, which directly affect the detection capability and tell us how sensitive our detection system can be and how close the real detection limit is to the theoretical calculation from Section 3. We will also perform other simulations and analysis of the existing topology, including frequency domain simulations, CMRR, PSRR, gain accuracy, etc. We intend to continue work on building an even more complex topology which includes AD conversion. Furthermore, we will compare the simulation results with experimental data in future studies.

6 References

1. D. Strle, B. Štefane, M. Trifkovič, M. Van Miden, I. Kvasić, E. Zupančič and I. Mušević, Chemical Selectivity and Sensitivity of a 16-Channel Electronic Nose for Trace Vapour Detection, *Sensors*, Volume 17, Issue 12, 8 December 2017, 2845.
2. A. Gradišek, M. Midden, M. Koterle, V. Prezelj, D. Strle, B. Štefane, H. Brodnik, M. Trifkovič, I. Kvasić, E. Zupančič and I. Mušević, Improving the Chemical Selectivity of an Electronic Nose to TNT, DNT and RDX Using Machine Learning, *Sensors*, Volume 19, Issue 23, 27 November 2019.
3. D. Strle, B. Štefane, E. Zupančič, M. Trifkovič, M. Maček, G. Jakša, I. Kvasić and I. Mušević, Sensitivity Comparison of Vapor Trace Detection of Explosives Based on Chemo-Mechanical Sensing with Optical Detection and Capacitive Sensing with Electronic Detection, *Sensors*, Volume 14, Issue 7, 27 June 2014, 11467-11497.
4. M. Trifkovič, D. Raič, D. Strle, Digital Signal processing for a Multi Channel Chemical Sensor Interface, *Informacije MIDEM*, Vol. 45, No. 3 (2015), 195-203.
5. D. Strle, J. Trontelj, B. Štefane, I. Mušević, Sensor System for Vapor Trace Detection of Explosives, *SENSORS, 2012 IEEE*, 2012, pp. 1-4.
6. D. Strle et al., „Surface-Functionalized COMB Capacitive Sensors and CMOS Electronics for Vapor Trace Detection of Explosives,” in *IEEE Sensors Journal*, Vol. 12, no. 5, May 2012. pp. 1048-1057.
7. A. Tuševski, A. Gradišek, D. Strle, Selectivity of Vapour Trace Detection System, *IEEE International Symposium on olfaction and Electronic Nose*, Aveiro, June 1, 2022

8. Qinwen Fan, Fabio Sebastiano, Johan H. Huijsing and Kofi A. A. Makinwa, A 1.8uW 60nV/ $\sqrt{\text{Hz}}$ Capacitively-coupled Chopper Instrumentation Amplifier in 65 nm CMOS for Wireless Sensor Nodes, *IEEE Journal of Solid-State Circuits*, Vol. 46, Issue: 7, July 2011, 1534-1543.
9. Witte J.F, Makinwa K.A.A, Huijsing J. H, 2009, Dynamic Offset Compensated CMOS Amplifiers, Delft university of Technology, the Netherlands, Springer Science+Business Media B.V.
10. Q. Fan, J. H. Huijsing, and K. A. A. Makinwa, »A 21 nV/sqrt(Hz) chopper-stabilized multipath current-feedback instrumentation amplifier with 2uV offset«, in IEEE ISSCC Dig. Tech. Papers, 2010, pp. 80-81.
11. R. Wu, K. A. A. Makinwa, and J.H. Huijsing, »A chopper current-feedback instrumentation amplifier with a 1mHz 1/f noise corner and an AC-coupled ripple-reduction loop«, *IEEE J. Solid-State Circuits*, vol. 44, no.12, pp.3232-3243, Dec. 2009Q. Fan, J. H. Huijsing, and K. A. A. Makinwa, »A 21 nV/sqrt(Hz) chopper -stabilized multipath current-feedback instrumentation amplifier with 2uV offset,« in IEEE ISSCC Dig. Tech. Papers, 2010, pp. 80-81.
12. Thijs Rooijers, Shoubhik Karmakar, Yoshinori Kusuda, John H. Huijsing and Kofi A. A. Makinwa »A Fill-In Technique for Robust IMD Suppression in Chopper Amplifiers«, *IEEE JOURNAL OF SOLID-STATE+ATE CIRCUITS*, VOL. 56, NO. 12, DECEMBER 2021
13. Liang Fang and Ping Gui »A Low-Noise Low-Power Chopper Instrumentation Amplifier With Robust Technique for Mitigating Chopping Ripples«, *IEEE JOURNAL OF SOLID-STATE CIRCUITS*, VOL. 57, NO. 6, JUNE 2022



Copyright © 2024 by the Authors.
This is an open access article distributed under the Creative Commons Attribution (CC BY) License (<https://creativecommons.org/licenses/by/4.0/>), which permits unrestricted use, distribution, and reproduction in any medium, provided the original work is properly cited.

Arrived: 14. 05. 2024

Accepted: 25 .09. 2024